

Image reconstruction for compressed sensing based on joint sparse bases and adaptive sampling

Huihui Li¹ · Yan Zeng² · Ning Yang¹

Received: 6 May 2016 / Revised: 17 July 2017 / Accepted: 30 September 2017 / Published online: 19 October 2017
© Springer-Verlag GmbH Germany 2017

Abstract In this paper, we focus on tackling the problem that one sparse base alone cannot represent the different content of the image well in the image reconstruction for compressed sensing, and the same sampling rate is difficult to ensure the precise reconstruction for the different content of the image. To address this challenge, this paper proposed a novel approach that utilized two sparse bases for the representation of image. Moreover, in order to achieve better reconstruction result, the adaptive sampling has been used in the sampling process. Firstly, DCT and a double-density dual-tree complex wavelet transform were utilized as two different sparse bases to represent the image alternatively in a smoothed projected Landweber reconstruction algorithm. Secondly, different sampling rates were adopted for the reconstruction of different image blocks after segmenting the entire image. Experimental results demonstrated that the images reconstructed with the two bases were largely superior to that reconstructed with a single base, and the PSNR could be improved further after using the adaptive sampling.

Keywords Compressed sensing · Adaptive sampling · DCT · Double-density dual-tree complex wavelet transform

1 Introduction

Traditional signal processing methods need to sample the original signals according to the Nyquist Theorem for facilitating subsequent signal sample processing. When majority of the information is unnecessary, such traditional sampling method would waste much time and storage space. Therefore, it is particularly necessary to develop a new methodology for signal acquisition as widely used in various image analysis applications [1–5]. Recently, compressed sensing (CS) [6,7] has received more and more attention for that CS can achieve sampling and compression simultaneously while greatly reducing the sampling rate and storage space of digital signal acquisitions.

In CS research field, the precise reconstruction plays a critical role in the practical applications. Generally, the reconstruction of CS can be formulated as a non-convex l_0 norm problem, which is an NP-hard problem. Thus, the most common solution is to convert it into a l_1 norm problem [8] that could be solved by using some convex optimization algorithms. As for image reconstruction, prior knowledge of the image is exploited as the constraints for solving the l_1 norm problem, which could be solved with some optimization algorithms, such as the interior points method [9], alternate projections onto convex sets (POCS) [10], the iterative shrinkage thresholding algorithm [11], iteratively reweighted algorithms [12]. Among the optimization methods, the constraint condition is a key factor that affects the reconstruction precision. Thus far, the sparse representation of image has been commonly used as constraint, because a suitable sparse base could fully represent the image and ensure a high-quality reconstruction.

Currently, although the orthogonal wavelet base is popular for the image reconstruction of CS, it has obvious shortcomings. It lacks significant directional selectivity and the

✉ Yan Zeng
zengyan3925@163.com

Huihui Li
lihui@nwpu.edu.cn

¹ College of Automation, Northwestern Polytechnical University, Xi'an 710012, China

² Department of Automation Engineering, Tangshan Polytechnic College, Tangshan 063200, China

shift invariance which renders it unable to fully represent the image textures, profiles, and some geometrical features. Therefore, the orthogonal wavelet base is not the best choice. Rauhut et al. [13] has proved that redundant dictionaries could be utilized for image reconstruction. The main distinction is that Rauhut used an over-complete dictionary for the selection of atoms which results in the chosen atoms matching the image contents more accurately. Meanwhile, Mun et al. [15] employed the framework of block compressed sensing (BCS) [14] to reconstruct the images and also used different directional wavelets to characterize the image. In addition, the bivariate shrinkage algorithm [16, 17] was utilized in the multi-scale decomposition structure fashion to provide the sparsity constraints. In the work of [18], the Bandlet dictionary was treated as the sparse base.

Inspired by Mun’s work, the major contributions of our paper can be summarized as follows: (1) Taking advantage of two transforms, the 2-D discrete cosine transform (DCT) and the 2-D double-density dual-tree complex discrete wavelet transform (DDTCWT) [19], to represent the image alternately, which could better characterize the image compared with only single sparse transformation. (2) In order to achieve a high precision reconstruction, the adaptive sampling was integrated into the measurement for acquiring the specific information of different parts of image.

The remainder of this paper is organized as follows. In Sect. 2, a brief description is presented for the selected sparse bases. Then, the specific reconstruction is described in Sect. 3. The experimental results are shown and discussed in Sect. 4, and the conclusion is then presented in Sect. 5.

2 Sparse bases selection

As is known, different sparse bases could be used to represent different content of the image. In this paper, to better characterize the image, two bases were adopted to represent the texture and the edges in the image, respectively. Thus, the sparse representation with two sparse bases could be the constraint conditions in the image reconstruction.

Firstly, for the representation of image containing abundant texture information, the commonly used reversible transforms have mainly included DCT and wavelet atoms [20]. However, the spatial locality of wavelet atoms is very limited and its basis function has obvious wake phenomenon, which results in the artifact in reconstruction [21]. Consequently, the 2-DDCT was exploited to represent the texture of image in this paper. On the other hand, the DDDTCWT was adopted as the sparse base for the image edges representation. In particular, the DDDTCWT is a kind of DWT that combines the dual-tree DWT and the double-density DWT, and it apparently holds the characteristics and advantages of these

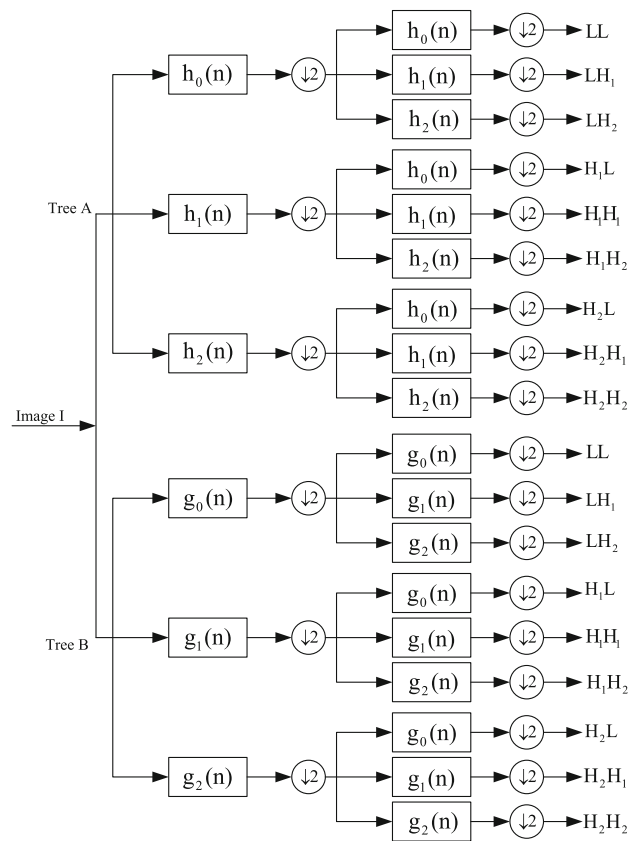


Fig. 1 Decomposition of an image based on the 2-D double-density dual-tree real DWT

two types of wavelets [22]. The principle of DDDTCWT is described briefly below.

The DDDTCWT presented in this paper is based on two scaling functions $\phi_h(t)$, $\phi_g(t)$, four distinct wavelets $\psi_{h,i}(t)$, $\psi_{g,i}(t)(i = 1, 2)$, and the wavelets satisfy the following rules:

$$\begin{aligned} \psi_{h,1}(t) &\approx \psi_{h,2}(t - 0.5) & (1) \\ \psi_{g,1}(t) &\approx \psi_{g,2}(t - 0.5) & (2) \\ \psi_{g,1}(t) &\approx H \{ \psi_{h,1}(t) \} & (3) \\ \psi_{g,2}(t) &\approx H \{ \psi_{h,2}(t) \} & (4) \end{aligned}$$

where H represents the Hilbert transform. It can be seen that the two wavelets $\psi_{h,i}(t)$ are offset from one to another by half, and the wavelets $\psi_{g,i}(t)$ and $\psi_{h,i}(t)$ form an approximate Hilbert transform pair. As the specific filter design procedure for the DDDTCWT described in [19], the emphasis would be put on the description of the process using the DDDTCWT for image decomposition and reconstruction. Figure 1 shows the decomposition of an image based on the 2-D double-density dual-tree real DWT.

In Fig. 1, $h_0(g_0)$, $h_1(g_1)$ and $h_2(g_2)$ indicate a low-pass filter, a first-order high-pass filter and a second-order high-



Fig. 2 Images used in the experiments

pass filter, respectively. The 2-D double-density dual-tree real DWT of an image is implemented by using two over-sampled 2-D double-density DWTs in parallel. Similarly, the DDDTCWT of the input image is implemented by four 2-D double-density DWTs in parallel. Thus, it can produce 32 oriented wavelets and lead to a more precise representation for

the image than traditional transforms. The primary properties of the DDDTCWT include: approximate shift invariance, directional selectivity, a redundancy of 4:1 along with invariance to different scales of the transform, and a similarity to a continuous wavelet transform. Obviously, all these properties are instrumental to the image reconstruction of CS.

Fig. 3 Image Lenna, Barbara, and Curtain reconstruction with a fixed sampling rate. **a** DCT, **b** DWT, **c** DDWT, **d** CT, **e** DDDTCWT, **f** DCT-DDDTCWT

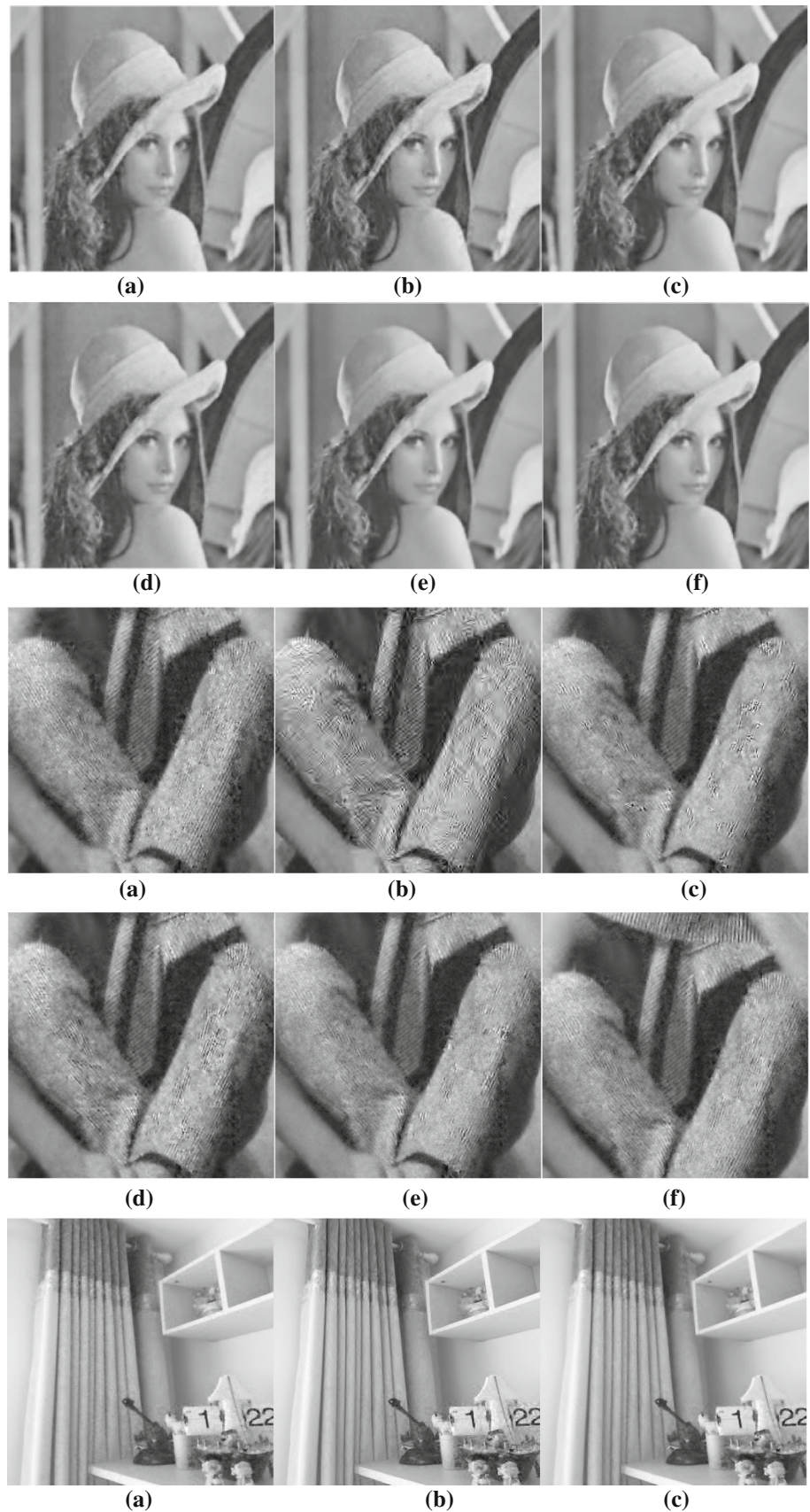


Fig. 3 continued

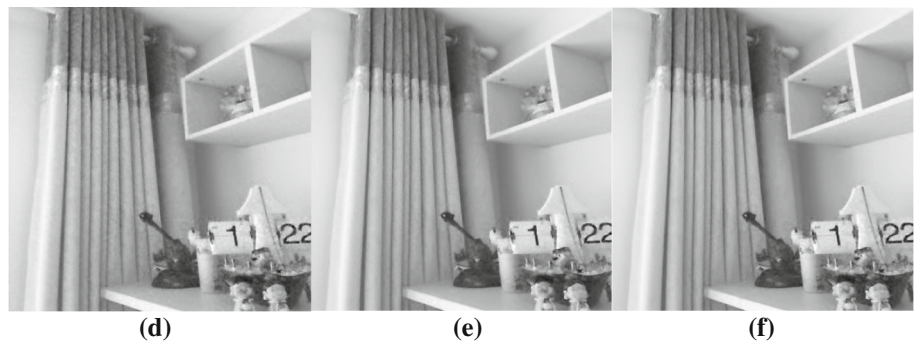


Table 1 PSNR performance of gray images based on different sparse bases

Sampling rate	0.1	0.2	0.3	0.4	0.5
Lena					
DCT	27.70	30.43	32.46	34.16	35.74
DWT	27.58	30.79	32.88	34.64	36.22
DDWT	28.06	31.15	33.25	35.10	36.64
CT	28.09	30.93	32.90	34.62	36.21
DDDCWT	28.21	31.43	33.49	35.22	36.84
DCT-DDDCWT	28.81	31.66	33.68	35.45	37.04
Barbara					
DCT	22.74	24.38	25.92	27.40	29.02
DWT	22.37	23.17	25.08	27.33	28.13
DDWT	22.59	24.25	25.69	27.07	28.72
CT	22.70	24.29	25.84	27.52	29.30
DDDCWT	22.72	24.30	25.74	27.29	28.81
DCT-DDDCWT	23.08	24.86	26.31	27.92	29.84
Goldhill					
DCT	26.16	28.32	29.46	31.24	32.56
DWT	26.74	28.47	30.21	31.00	32.94
DDWT	26.91	28.82	30.34	31.64	33.05
CT	26.79	28.87	30.47	31.89	33.25
DDDCWT	26.93	28.91	30.45	31.76	33.11
DCT-DDDCWT	27.02	29.01	30.57	31.95	33.47
Bird					
DCT	24.94	27.45	29.16	30.64	32.17
DWT	25.12	27.59	29.73	31.67	33.52
DDWT	25.31	27.80	29.66	31.31	32.94
CT	25.61	27.97	29.77	31.37	32.95
DDDCWT	25.26	27.72	29.6	31.28	32.95
DCT-DDDCWT	25.7	28.01	29.9	31.59	33.17
Clock					
DCT	24.71	28.03	30.36	32.56	34.55
DWT	24.50	27.71	30.98	34.11	37.12
DDWT	24.77	28.67	31.57	33.93	36.16
CT	25.32	28.57	30.95	33.10	35.09
DDDCWT	24.90	28.77	31.58	33.94	36.14
DCT-DDDCWT	25.94	29.43	32.10	34.36	36.49

Table 1 continued

Sampling rate	0.1	0.2	0.3	0.4	0.5
Curtain					
DCT	26.42	29.65	32.06	34.07	35.92
DWT	26.83	30.14	32.9	35.44	37.92
DDWT	26.62	30.44	32.88	34.92	36.84
CT	26.91	30.23	32.52	34.45	36.31
DDDCWT	27.09	30.7	33.08	35.14	37.09
DCT-DDDCWT	27.81	31.3	33.71	35.76	37.69

3 Image reconstruction

In the CS reconstruction, the model under the constraint condition of a signal's sparsity can be described as follows:

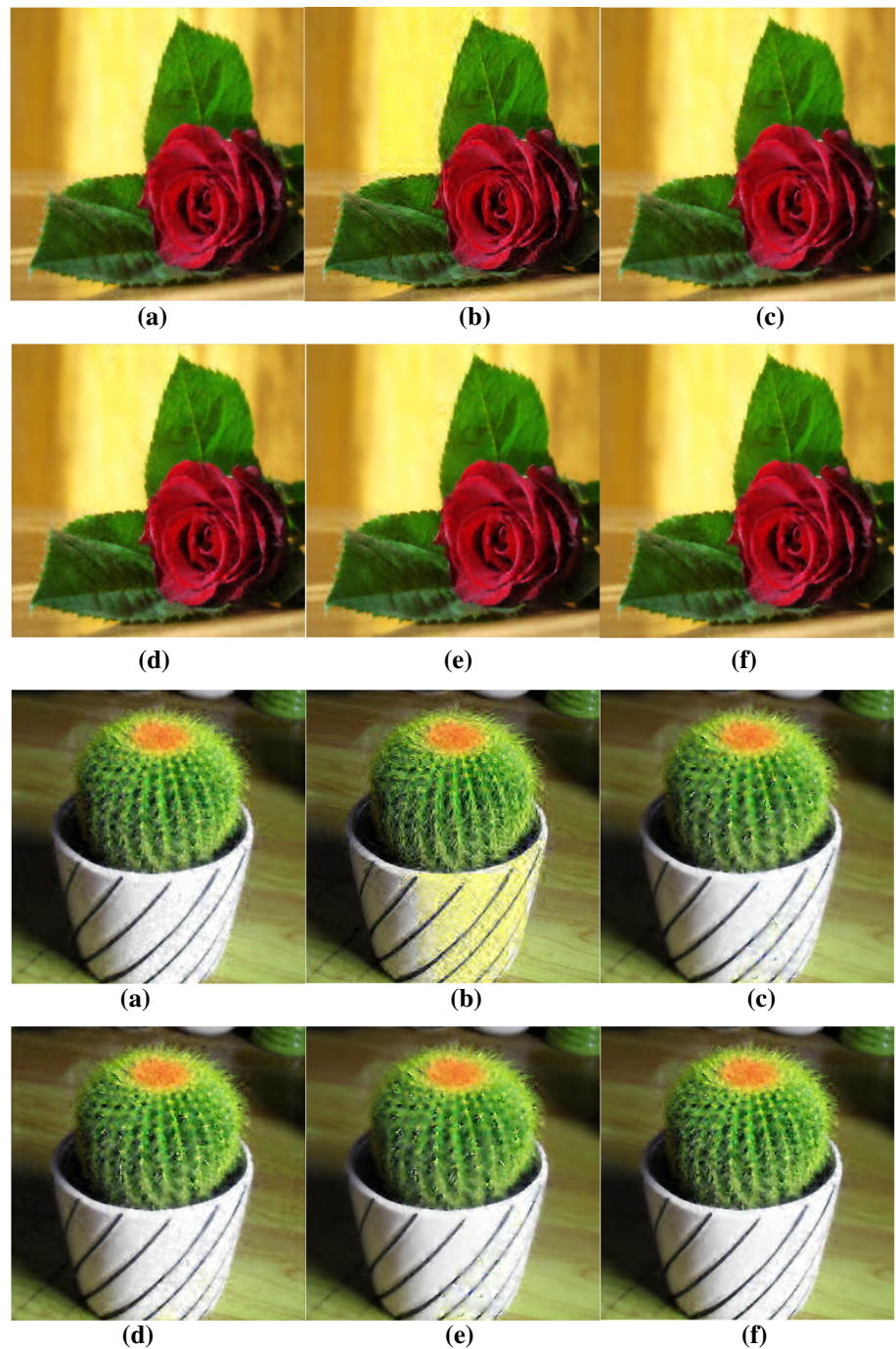
$$\min \|\Psi^H x\|_{l_1} \text{ s.t. } \Phi x = y \tag{5}$$

where $x \in R^{N \times 1}$ represents a discrete-time signal, $\Psi \in R^{N \times N}$ indicates the selected sparse base, y denotes the measured signal with a dimension of $M \times 1$, $\Phi \in R^{M \times N}$ is the measurement matrix which satisfies the RIP and can be obtained by random generation method [23]. In addition, the value of M/N is the sampling rate of CS. Herein, two sparse bases have been exploited to represent the image alternately, and the model can be described as:

$$\min \|\Psi_i^H x\|_{l_1} \text{ s.t. } \Phi x = y \tag{6}$$

where $i = 1, 2$, Ψ_1 and Ψ_2 indicate DCT and DDDTCWT, respectively. In order to use the framework of BCS and the smoothed projected Landweber reconstruction (SPL) algorithm for solving this question, Φ is constructed by Φ_B , and Φ_B is the measurement matrix for each image block after the segmentation. Concretely, the core of this paper's reconstruction method will be presented in the next two parts: *the reconstruction algorithm based on DCT and DDDTCWT, the entire reconstruction process integrated with the adaptive sampling.*

Fig. 4 Image Rose, Plant reconstruction with a fixed sampling rate. **a** DCT, **b** DWT, **c** DDWT, **d** CT, **e** DDDTCWT, **f** DCT-DDDTCWT



3.1 The reconstruction algorithm based on DCT and DDDTCWT

To solve Eq. (5), Gan [14] and Mun [15] proposed the SPL algorithm which has been used widely. The algorithm starts from an approximative image, which is obtained from the measured vectors and corrupted by noises initially; then, the corrupted image is optimized by the iterative projecting and the thresholding to get the optimal image. In particular, the

optimization process can be summarized: Initially project the vectors gained from the last iteration onto a convex set to obtain the new vectors; then, arrange the new vectors to form a new image; finally, apply the thresholding based on a sparse base to get the optimal results. Obviously, it can be seen that the projection and the thresholding are very important for the reconstruction. However, the thresholding has a close relationship with the used sparse base. Thus, the used sparse base is a key factor for the reconstruction of CS. The work of

Table 2 PSNR performance of color images based on different sparse bases

Sampling rate	0.1	0.2	0.3	0.4	0.5
Rose					
DCT	29.00	32.17	34.38	36.23	37.89
DWT	26.54	32.05	34.74	36.81	38.62
DDWT	29.32	33.15	35.55	37.54	39.33
CT	29.48	32.73	34.99	36.89	38.59
DDDCWT	29.32	33.06	35.44	37.42	39.22
DCT-DDDCWT	30.03	33.42	35.73	37.65	39.39
Plant					
DCT	22.46	24.24	25.60	26.94	28.41
DWT	19.13	22.67	25.00	26.31	27.94
DDWT	21.49	24.13	25.95	27.56	29.23
CT	22.25	24.42	25.94	27.30	28.80
DDDCWT	21.50	24.22	26.05	27.60	29.26
DCT-DDDCWT	22.99	24.86	26.44	27.96	29.60
Panda					
DCT	23.51	26.17	28.10	30.01	31.90
DWT	20.06	24.37	28.17	30.35	32.14
DDWT	23.23	29.97	29.08	30.99	32.76
CT	23.61	26.63	28.58	30.42	32.17
DDDCWT	23.47	26.74	28.70	30.48	32.18
DCT-DDDCWT	24.34	27.01	28.89	30.64	32.31

[15] has proved that the SPL algorithm can solve Eq. (5) with single sparse base. Considering the complexity of images, an effort was made to embed DCT and DDDTCWT into the SPL algorithm synchronously for solving Eq. (6). Thus, the thresholding will be performed in both DCT domain and DDDTCWT domain alternately to get the optimal results.

In addition, it is needed to segment the entire image into many image blocks before the sampling for fast processing and memory saving. Thus, the dimension of measurement matrix Φ_B which satisfies the RIP similarly should match the dimension of each image block. The algorithm is described below.

Input The $M \times B^2$ measurement matrix for each image block whose dimension is $B \times B$ is designated as Φ_B , it satisfies $\Phi_B^T \cdot \Phi_B = \mathbf{I}$ and can be obtained by the random generation method as described in [15]. The vector obtained from a image measurement by arranging all of its elements into a column is designated as y_i , $i = 1, 2, \dots, L^2/(B \times B)$, $L \times L$ is the original image's dimension. The convergence threshold to stop the iterations is designated as ε . The number of maximum iterations allowed is designated as j_{\max} .

Initialization Compute $\tilde{x}_i = \Phi_B^+ \cdot y_i$ for each image block, then, convert and combine each vector \tilde{x}_i to construct an initial image x_0 . Additionally, set the iteration time $j = 0$;

Repetitions Iterate on the j th time.

- (1) Divide the image x_1 obtained from the latest iteration into a set of non-overlapping image blocks x_i . Convert each x_i into a 1-dimensional vector x_i' , and calculate the optimized vector x_i'' as $x_i'' = x_i' + \Phi_B^T (y_i - \Phi_B x_i')$. Then, generate the image x_2 by combining all the optimized vectors.
- (2) Use DCT to transform image x_2 , yielding f and processing it with a hard threshold. After that, the inverse DCT is applied to generate image x_3 for the next step.
- (3) Optimize the image x_3 to obtain a new image x_4 . Note that the detailed optimization procedure is same as Step (1).
- (4) Use DDDTCWT to decompose image x_4 and yield coefficient f_1 . Then, implement the thresholding, and obtain image x_5 through the inverse DDDTCWT. This process seems very similar to Step (2) at first glance, nevertheless, there existing differences in terms of the thresholding. The bivariate shrinkage is adopted in the thresholding for f_1 as it can exploit the statistical dependency between the transform coefficients and their corresponding parents' coefficients (the upper level coefficients) and is more appropriate for the directional transforms. Specifically, the bivariate shrinkage is performed in the DDDTCWT domain, which is almost identical to the application in the dual-tree DWT (DDWT) domain, except that more sub-bands are needed to be handled.
- (5) Remove the blocking artifacts of image x_5 by using the Wiener filter. The image x_6 is the result after filtering.
- (6) Calculate $E_j = \frac{1}{\sqrt{N}} \|x_6 - x_1\|_2$ and determine whether $|E_j - E_{j-1}| < \varepsilon$ or $j > j_{\max}$ is satisfied. Here, E_{j-1} represents the MSE between x_6 and x_1 , which is calculated in the $(j-1)$ th iteration. If the condition is met, the optimization will stop, otherwise, designate $j = j + 1$ and enter the next iteration.

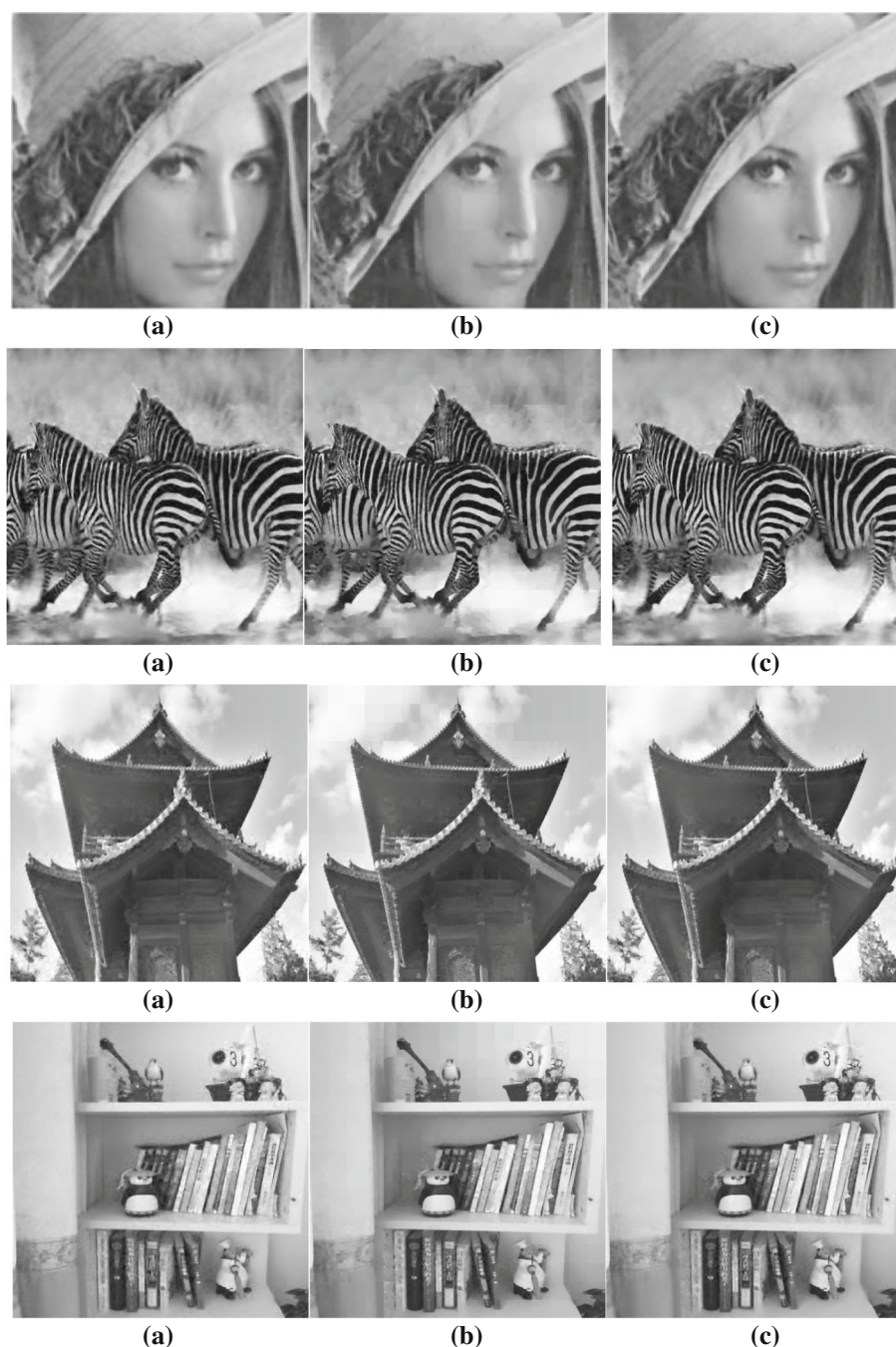
Output The reconstructed image $x_{\text{rec}} = x_6$.

Obviously, the improvement in the SPL algorithm of this paper just change the sparse bases and does not change the essence of the algorithm (the projection method); thus, the algorithm of this paper can realize the image reconstruction at the preliminary analysis. The specific experimental validation is displayed in the next section.

3.2 The entire reconstruction process integrated with the adaptive sampling

It is known that the smoother the image block is, the greater its sparsity is. Generally, only a small amount of measurement information is required to achieve a precise reconstruction. On the contrary, a larger amount of measurement information would be needed for the reconstruction of an image block

Fig. 5 Image Lena, Zebra, Temple, and Bookcase reconstruction utilizing different methods. **a** DCT-DDDTCWT, **b** adaptive-TV, **c** this paper's methodology



with rich detail information. Thus, it can give a revelation whether the image can be reconstructed in the different sampling rates. For the smooth part of the image, a low dimension matrix can be used to measure it, while a high dimension matrix can be used to measure the non-smooth part of the image. If there is just one measurement matrix is used in the reconstruction, the sampling rate is difficult to set. The low sampling rate will lower the overall reconstruction precision,

while the higher sampling rate will be not very necessary for the reconstruction of the smooth part in image. Thus, in this way, it is easy to balance the reconstruction precision and can make both the smooth part and the non-smooth part of the image achieve a higher reconstruction precision theoretically.

However, there exists one question: how to distinguish the image's smooth and non-smooth part? It is known the

Table 3 PSNR performance of gray image utilizing different methods

Method	Image	0.1	0.2	0.3	0.4	Image	0.1	0.2	0.3	0.4
DCT-DDDTCWT	Lena	28.81	31.66	33.68	35.45	Barbara	23.08	24.69	26.16	27.75
Adaptive-TV		28.57	31.50	33.75	35.68		22.62	23.99	25.32	26.70
Our method		29.64	32.87	35.04	36.80		23.44	25.59	27.52	29.21
DCT-DDDTCWT	Pepper	29.19	32.03	33.74	35.10	Zebra	20.50	23.85	26.6	29.03
Adaptive-TV		28.77	32.04	33.93	35.38		20.49	24.28	27.05	29.55
Our method		29.95	32.60	34.20	35.50		21.6	25.48	28.46	31.01
DCT-DDDTCWT	Home	26.84	29.81	31.92	33.70	Temple	24.98	27.78	29.85	31.78
Adaptive-TV		27.08	30.15	32.25	34.02		26.02	29.32	32.08	34.64
Our method		27.92	30.84	32.89	34.63		26.19	29.43	32.07	34.65
DCT-DDDTCWT	Cat	27.36	30.31	32.48	34.51	Bookcase	24.79	27.87	30.13	32.12
Adaptive-TV		27.18	30.70	32.81	35.35		25.29	28.64	31.37	33.91
Our method		28.49	31.90	34.56	37.18		25.93	29.30	31.79	34.08

image is needed to be segmented in the reconstruction as mentioned before, thus considering these factors comprehensively the block-based sampling approach can be adopted. That means, the image can be divided into many blocks firstly; then, classify all the blocks into two types according to their smoothness; lastly, use different matrixes to measure and reconstruct the blocks.

In particular, the classification principle is based on the variance of image blocks [24]. The threshold T is designated as $T = p \cdot (\sigma_{\max}^2 - \sigma_{\min}^2) + \sigma_{\min}^2$, where σ_{\max} and σ_{\min} indicate the maximum and minimum value of all blocks' variance, respectively, and p is an adjustable parameter. The two measurement matrices designed for the smooth blocks and the non-smooth blocks are Φ_{Bl} and Φ_{Bh} , respectively. The method of generating Φ_{Bl} and Φ_{Bh} is same as that of generating Φ_B , and the process to make sure the dimension of Φ_{Bl} and Φ_{Bh} is described below.

Firstly, the sampling rate for smooth blocks is defined as s_1 , and the other sampling rate for non-smooth blocks is s_2 . If s is the average sampling rate for the entire image, it will satisfy $n_0s = n_1s_1 + n_2s_2$, n_0 is the total number of all blocks, n_1 is the number of smooth blocks, n_2 is the number of non-smooth blocks. Then, make sure n_1 and n_2 by adjusting the parameter p . Obviously, if s , n_0 , n_1 , n_2 are known, it is easy to find the range of s_1 and s_2 . (In this paper, make $s_2 = 2s_1$ and $n_1 = n_2$ for determining s_1 and s_2 easily.) If s_1 and s_2 are known, the dimension of Φ_{Bl} and Φ_{Bh} will be made sure.

After obtaining Φ_{Bl} and Φ_{Bh} , the specific information of the original image can be acquired. Then, the algorithm described in Sect. 3 is employed to reconstruct the image. However, it should be noted that the optimization process is not identical to that mentioned above. The difference is primarily in the initialization, in both Steps (1) and (3), where Φ_B is replaced by Φ_{Bl} and Φ_{Bh} in each iteration. The same

implementation occurs in the other steps, so it will not take too much description here. The specific experimental evaluation is provided in the next section.

4 Experiments

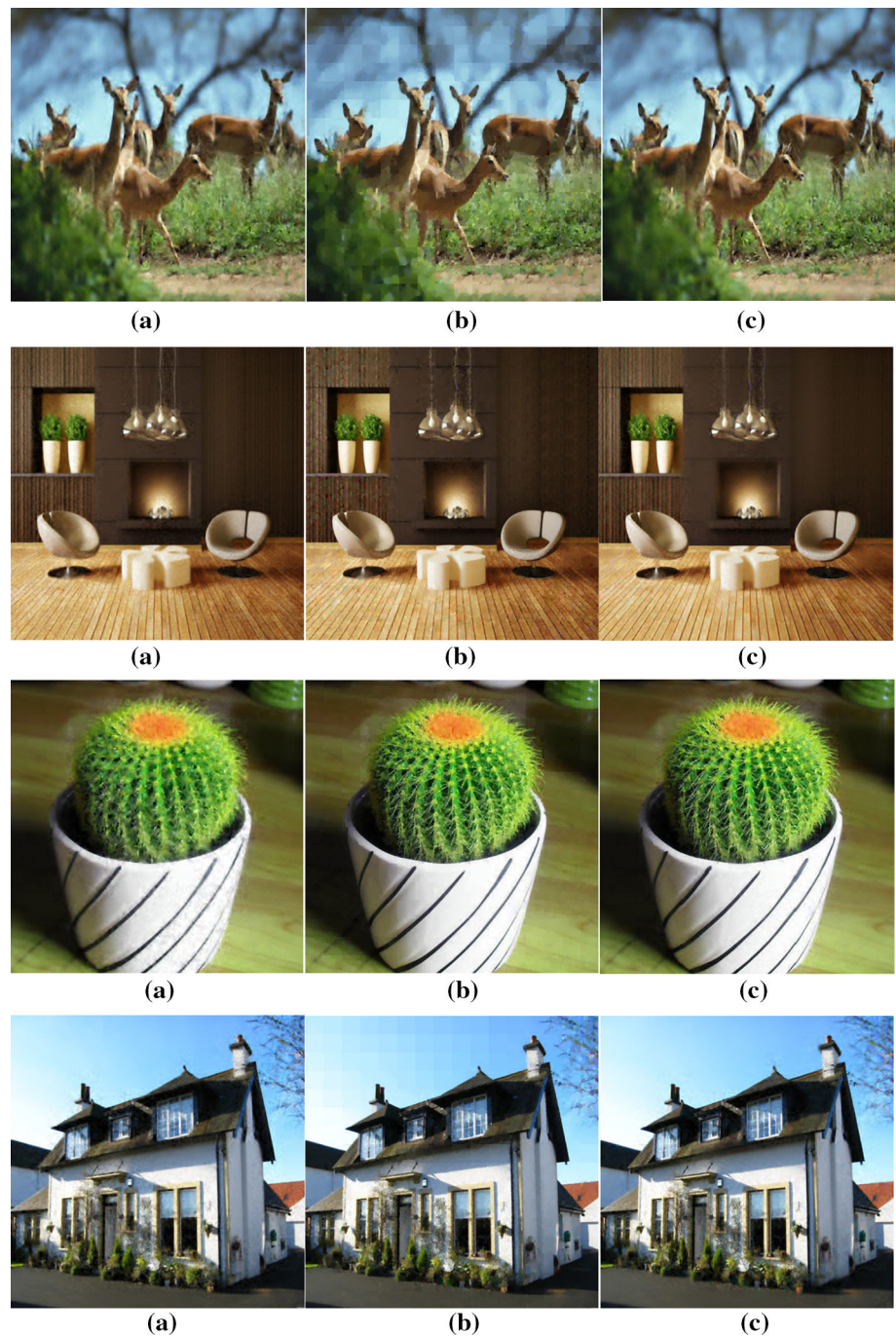
Several experiments were performed to evaluate the proposed method. These experiments could be divided into two classes based on whether the adaptive sampling was integrated into the reconstruction or not. In addition, all the random measurement matrices selected were orthonormal in this paper, the stopping parameter was set as $\varepsilon = 0.001$, and the dimension of all the experiment images was 512×512 . Figure 2 shows all the images used in the experiments.

4.1 The first experiment

In order to evaluate the impact of different sparse bases for reconstruction, DCT, DWT, DDWT, CT, DDDTCWT were deployed, along with the combination of DCT and DDDTCWT (DCT-DDDTCWT) in the reconstruction. Further, this experiment was divided into two groups according to the type of images. In the first group, some gray images were reconstructed, and the color images were reconstructed in the second group. Specifically, for the reconstruction of color image, the image was decomposed into three channels (R, G, B) firstly, secondly the image was reconstructed in different channels, and lastly the reconstructed results were combined into one image.

Figure 3 illustrates the visual reconstruction results for the gray images: Lena, Barbara, and Curtain, and the sampling rates of different images are 0.1, 0.2, 0.2, respectively. As can be seen, the blocking artifacts are apparent in the images

Fig. 6 Images Deer, Furniture, Plant, and House reconstruction utilizing different methods. **a** DCT-DDDTCWT, **b** adaptive-TV, **c** this paper's methodology



obtained by the BCS and the iterative projection algorithms along with DCT, DWT, and CT, even though the Wiener filtering has been applied in the process. On the other hand, the results obtained by integrating DDWT or DDDTCWT could eliminate the blocking artifacts efficiently and provide a superior visual effect. However, the reconstruction images based on DDDTCWT become too smooth, and the texture part of these images becomes blurry. The algorithm described in Sect. 3 achieves a better performance compared to the former.

Thus, the results demonstrate that the proposed algorithm can reconstruct the texture and edges of image synthetically. In addition, Table 1 shows the PSNR of different reconstruction images at different sampling rates ranging from 0.1 to 0.5. In this table, the maximum value for each set of comparison results is bolded. It is evident that the algorithm combined with DCT and DDDTCWT simultaneously is competitive in the image reconstruction.

Table 4 PSNR performance of color image utilizing different methods

Method	Image	0.1	0.2	0.3	0.4	Image	0.1	0.2	0.3	0.4
DCT-DDDTCWT	Red House	20.70	23.31	25.09	26.67	FlowerHouse	21.80	24.05	25.71	27.26
Adaptive-TV		20.89	23.78	25.92	27.73		21.94	24.56	26.67	28.49
Our method		21.69	24.42	26.23	27.73		22.43	24.74	26.50	28.02
DCT-DDDTCWT	House	23.88	26.47	28.38	30.09	Cup	27.01	30.29	32.87	35.31
Adaptive-TV		23.99	26.89	29.11	31.12		28.22	31.87	34.92	37.57
Our method		24.71	27.37	29.34	31.10		28.42	32.20	35.37	38.21
DCT-DDDTCWT	Corner	26.94	30.04	32.45	34.57	Furniture	24.94	26.87	28.38	29.86
Adaptive-TV		27.64	31.01	33.65	35.87		24.91	27.31	29.50	31.42
Our method		27.92	31.14	33.65	35.89		25.84	28.20	29.94	31.40
DCT-DDDTCWT	Panda	24.34	27.01	28.89	30.64	Rose	30.03	33.42	35.73	37.65
Adaptive-TV		24.53	27.55	30.10	32.43		30.51	34.00	36.44	38.54
Our method		25.29	28.15	29.33	32.36		30.82	34.74	37.14	39.15
DCT-DDDTCWT	Plant	22.99	24.86	26.44	27.96	Deer	24.19	26.53	25.29	29.82
Adaptive-TV		23.33	25.57	27.55	29.70		23.93	26.44	28.41	30.35
Our method		23.67	25.97	28.09	30.49		24.82	27.31	29.37	31.33

Figure 4 illustrates the visual reconstruction results for the color images: Rose, Plant. The sampling rates of different images are 0.1, 0.2, respectively. Obviously, the images reconstructed by the first five kinds of sparse bases contain more noise. Especially when the sparse base is DWT, the reconstruction results are very poor. Table 2 shows the PSNR of different reconstruction images at different sampling rates ranging from 0.1 to 0.5. In this table, the maximum value for each set of comparison results is also bolded as in Table 1. The results are similar to that of the gray images, the algorithm integrated with DCT and DDDTCWT can raise the PSNR further, especially when the sampling rate is relatively low.

Therefore, all the results of the first experiment have proved that the algorithm of this paper is very competitive in the reconstruction of both the gray images and color images, especially for the content-rich image reconstruction.

4.2 The second experiment

In this experiment, this paper's method based on the adaptive sampling and the joint sparse bases was compared with the method mentioned in the first experiment. Meanwhile, another approach known as "adaptive-TV" was also added to the comparison, which means the iterative projection algorithm was replaced by the minimum TV optimization algorithm in Candes's work [25]. In addition, this experiment was also divided into two groups: the gray image reconstruction and the color image reconstruction.

When the sampling rate is 0.2, the experimental results are displayed in Fig. 5. It is noted that the blocking artifacts are extremely severe in Fig. 5b, because the optimization is performed on each image block separately and the smooth-

ing is not added to the reconstruction process, even though the adaptive sampling has been utilized. Further, comparing the results obtained from the other two methods, it can be seen that the reconstruction precision is improved after using the adaptive sampling, and the most distinct improvement is that the texture part of each image is clearer. Table 3 provides the objective evaluation of reconstruction for the three methods. Likewise, the maximum value in each set of comparison results is also bolded. Obviously, the results are consistent with the visual results. The PSNR of image reconstructed by this paper's method could be increased by 2.3 dB, compared with the PSNR of image reconstructed based on "adaptive-TV". Furthermore, comparing the results of this paper's method with that of the method integrated with a fixed sampling, the adaptive sampling can improve the PSNR of image about 1 dB effectively. Thus, it illustrates that the adaptive sampling is conducive to the reconstruction of a higher-quality gray image.

Figure 6 illustrates the visual reconstruction results for the color images: Deer, Furniture, Plant, and House. The sampling rates for different images are 0.1, 0.2, 0.2, 0.2. Obviously, Fig. 6c is clearer than Fig. 6a, b in each image group, the blocking artifacts are extremely severe in Fig. 6b, and the reconstruction results are similar to that of the gray images. In addition, Table 4 displays the objective evaluation and the significance of the bold font in this table is same as the previous tables. Clearly, this paper's method can increase the PSNR of color image by about 1 dB on average, compared with the PSNR of image reconstructed by "adaptive-TV". Therefore, the paper's method is effective for the reconstruction of gray images and color images, and it is the most competitive in the three methods.

5 Conclusion

Considering the influences of different sparse bases and the adaptive sampling for image reconstruction in CS, this paper has proposed a new reconstruction method employing the adaptive sampling and an SPL algorithm integrated with DCT and DDDTCWT simultaneously. Experimental results show that, in most cases, the optimization algorithm based on DCT and DDDTCWT performs better than that based on one sparse base alone. Moreover, the reconstruction integrated with the adaptive sampling mentioned above can lead to the higher-quality image reconstruction. However, there remain many issues regarding this paper's method to be studied in the future. One example would be how to optimize the adaptive sampling further to improve the reconstruction precision.

Acknowledgements H.H.Li was supported by the National Science Foundation of China under Grant 60802084, Aero-Science Fund 20131953022, and the Fundamental Research Funds for the Central Universities 3102014JCQ01062.

References

1. Yao, X.W., Han, J., Zhang, D.W., Nie, F.P.: Revisiting co-saliency detection: a novel approach based on two-stage multi-view spectral rotation co-clustering. *IEEE Trans. Image Process.* **26**(7), 3196–3209 (2017)
2. Yao, X.W., Han, J., Gong, C., Qian, X.M., Guo, L.: Semantic annotation of high-resolution satellite images via weakly supervised learning. *IEEE Trans. Geosci. Remote Sens.* **54**(6), 3660–3671 (2016)
3. Yuan, Y., Meng, M.Q.H.: A novel feature for polyp detection in wireless capsule endoscopy images. In: *IEEE/RSJ International Conference on Intelligent Robots and Systems (IROS)*, pp. 5010–5015 (2014)
4. Cheng, G., Zhou, P., Han, J.: Learning rotation-invariant convolutional neural networks for object detection in VHR optical remote sensing images. *IEEE Trans. Geosci. Remote Sens.* **54**(12), 7405–7415 (2016)
5. Cheng, G., Han, J., Lu, X.Q.: Remote sensing image scene classification: benchmark and state of the art. *Proc. IEEE.* **105**(10), 1865–1883 (2017)
6. Donoho, D.: Compressed sensing. *IEEE Trans. Inf. Theory* **52**(4), 1289–1306 (2006)
7. Candès, E., Wakin, M.: An introduction to compressive sampling. *IEEE Signal Process. Mag.* **25**(2), 21–30 (2008)
8. Donoho, D., Elad, M., Temlyakov, V.: Stable recovery of sparse overcomplete representations in the presence of noise. *IEEE Trans. Inf. Theory* **52**(1), 6–18 (2006)
9. Kim, S., Koh, K., Lustig, M., et al.: An interior-point method for large-scale l_1 regularized least squares. *IEEE J-STSP* **1**(4), 606–617 (2007)
10. Candès, E., Romberg, J.: Signal recovery from random projections. In: *Proceedings of International Conference on SPIE.*, San Jose, CA, March 2005, pp. 76–86 (2005)
11. Beck, A., Teboulle, M.: A fast iterative shrinkage thresholding algorithm for linear inverse problems. *SIAM J. Imaging Sci.* **2**(1), 183–202 (2009)
12. Chartrand, R., Yin, W.: Iteratively reweighted algorithms for compressive sensing. In: *Proceedings of International Conference on Acoustics, Speech and Signal Processing*, Las Vegas, NV, March 2008, pp. 3869–3872 (2008)
13. Rauhut, H., Schnass, K., Vandergheynst, P.: Compressed sensing and redundant dictionaries. *IEEE Trans. Inf. Theory* **54**(5), 2210–2219 (2008)
14. Gan, L.: Block compressed sensing of natural images. In: *Proceedings of International Conference on Digital Signal Processing*, Cardiff, UK, July 2007, pp. 403–406 (2007)
15. Mun, S., Fowler, J.: Block compressed sensing of images using directional transforms. In: *Proceedings of International Conference on Image Processing*, Cairo, Egypt, Nov. 2009, pp. 3021–3024 (2009)
16. Selesnick, I., Baraniuk, R., Kingsbury, N.: The dual-tree complex wavelet transform. *IEEE Signal Process. Mag.* **22**(6), 123–151 (2005)
17. Sendur, L., Selesnick, I.: Bivariate shrinkage functions for wavelet-based denoising exploiting interscale dependency. *IEEE Trans. Signal Process.* **50**(11), 2744–2756 (2002)
18. Peyre, G.: Best basis compressed sensing. *IEEE Trans. Signal Process.* **58**(5), 2613–2622 (2010)
19. Selesnick, I.: The double-density dual-tree DWT. *IEEE Trans. Signal Process.* **52**(5), 1304–1314 (2004)
20. Demanet, L., Ying, L.: Wave atoms and sparsity of oscillatory patterns. *Appl. Comput. Harmon. Anal.* **23**(3), 368–387 (2007)
21. Lian, Q., Chen, S.: Image reconstruction for compressed sensing based on the combined sparse image representation. *Acta Autom. Sin.* **36**(3), 385–391 (2010)
22. Selesnick, I.: *Wavelets in Signal and Image Analysis*, 1st edn, pp. 39–66. Springer, Dordrecht (2001)
23. Candès, E.: The restricted isometry property and its implications for compressed sensing. *Comptes Rendus Math.* **346**(9), 589–592 (2008)
24. Nana, W., Jingwen, L.: Block adaptive compressed sensing of SAR images based on statistical character. In: *Proceedings of International Conference of Geoscience and Remote Sensing Symposium*, Vancouver, BC, July 2011, pp. 640–643 (2011)
25. Candès, E., Romberg, J., Tao, T.: Stable signal recovery from incomplete and inaccurate measurements. *Commun. Pure Appl. Math.* **59**(8), 1207–1223 (2006)



Huihui Li She received bachelor degree from Kunming University of Science and Technology in 2003, and master degree in 2003 and PhD in 2006 both from Northwestern Polytechnical University. Now she is an associate professor in College of Automation, Northwestern Polytechnical University. Her research interests are digital image processing, multiscale geometric analysis, etc. E-mail: lihuihui@nwpu.edu.cn.



Yan Zeng She received bachelor degree from Lanzhou University of Technology in 2011 and master degree from Northwestern Polytechnical University in 2014. Now she is a lecturer in Department of Automation Engineering, Tangshan Polytechnic College. Her research interests are digital image processing, compressed sensing, etc. E-mail: zengyan3925@163.com.



Ning Yang She received PhD in 2011 from Northwestern Polytechnical University. Now she is an associate professor in College of Automation, Northwestern Polytechnical University. Her research interests are digital image processing, computer vision, etc.